PERGAMON

International Journal of Multiphase Flow 26 (2000) 1797–1830

International Journal of Multiphase Flow

www.elsevier.com/locate/ijmulflow

Statistical method to calculate local interfacial variables in two-phase bubbly flows using intrusive crossing probes

S.G. Dias [a], F.A. França [b,*], E.S. Rosa [b]

[a] *Exploration and Production Department, Petrobras, Av. República do Chile 65, 20035-900 Rio de Janeiro RJ, Brazil*
[b] *Faculty of Mechanical Engineering, State University of Campinas, UNICAMP 13081-970, Campinas SP, Brazil*

Received 1 January 1998; received in revised form 4 November 1999

Abstract

This paper presents a statistical method to calculate local interfacial variables in two-phase gas–liquid bubbly flows from data taken with double-sensor intrusive probes. Firstly, one derives the geometrical relationship existing between the apparent and actual bubble velocity for a single spherical bubble flowing in a multidimensional flow field. The apparent variables are obtained from the experimental data when one assumes that the bubble trajectory is aligned with the probe axis. A similar relationship exists for the intersected chord length and bubble diameter. Then, the analysis is extended to a swarm of bubbles. The ratio between the apparent to the actual bubble velocity and the intersected chord length to the bubble diameter appear now as probability density functions. The experimental data were taken for air–water bubbly flow regime in a vertical round pipe with a double tip electrical probe. Processing the phase density function generated by the bubble events, one determines distribution function of the bubble velocity and intersected chord length, termed the apparent distributions. The variables of interest, actual bubble velocity and diameter, come out of the solution of a linear system of equations relating the probability function of the measured and estimated bubble velocity and bubble size ratio. The probability density function of the actual bubble velocity and bubble diameter, plus the bubble frequency, add up to various interfacial properties calculated with this technique: the void fraction, the bubble velocity, the bubble size, the interfacial area density and the interface velocity fluctuation intensity. To validate the method, the paper compares local and area averaged quantities with previously published results, volumetric measurements and extensively used correlation.

Keywords: Bubbly flow; Interfacial variables; Local void fraction; Bubble size and bubble velocity distribution; Double-sensor probe; Electrical probe

* Corresponding author. Tel:. +55-19-788-3262; fax: +55-19-289-3722.
E-mail address: ffranca@fem.unicamp.br (F.A. França).

0301-9322/00/$ - see front matter
PII: S0301-9322(99)00111-1

1. Introduction

Intrusive crossing probes were the first and, in many instances, the only experimental technique used to study the detailed spatial distribution of local variables in two-phase flows. Specifically in bubbly flow, electrical and optical probes and hot wire anemometer were widely used to measure the local void fraction, bubble size and frequency, interfacial velocity, area density and their spatial distribution (Serizawa et al., 1975a, 1975b; Lopez de Bertodano, 1992; Delhaye and Galaup, 1974).

When measuring variables in a vertical bubbly flow, with local void fractions attaining values as high as 20%, as one does in this work, it is inevitable that an intrusive probe method must be used. The intrusive probe, when inserted in the flow, pierces the dispersed gas bubbles and senses the phase change around its tip using different physical processes. They are (1) the variation of the electrical properties; (2) the variation of the refraction index, and (3) the change on the heat transfer coefficient, respectively, if one considers the electrical and optical probes or the hot wire anemometer. However, intrusive probes disturb the flow. Alternatives are the non-intrusive techniques, like the ultrasonic Doppler (Hilgert and Hoffmann, 1986), the state of the art Laser Doppler Velocimetry (LDV), or the Particle Image Velocimetry (PIV), and related photographic methods (Bachalo, 1994), which have been increasingly used. These non-intrusive techniques, despite being expensive, lack applications when the void fraction increases and the sound or the light beam has to cross a vast number of interfaces to reach the measurement volume.

Direct measurement of the time period for which the tip of the probe stays inside the gas bubble and that of the time interval the gas–liquid interface takes to travel between the two tips of a double-sensor probe, lead to the measurement of void fraction, bubble size and frequency, interface (bubble) velocity and interfacial area density. Following this line, Herringe and Davis (1976) developed an analysis relating the statistical distribution of a spherical bubble size to its measured chord length. The translation of the statistical parameters depended upon the bubble velocity, as measured by the probe. Recently, Liu and Clark (1995) presented an approach linking the statistical distribution of the bubble size to the chord length of the less restrictive ellipsoidal and ellipsoidal–truncated bubbles. In both papers the method is limited in a sense that the authors assume one-directional bubble trajectory, which is, ultimately, aligned with the probe axis. In a multidimensional bubbly flow, several forces and bubble-fluid interaction impose a spatial bubble trajectory. The bubble trajectory is not necessarily aligned with the axis of the probe. This misalignment is represented by an entrance angle, giving rise to an apparent bubble velocity. The apparent velocity, as measured by the probe, may be different from the actual bubble velocity. The first attempt to account for the entrance angle effect was proposed by Kataoka et al. (1986) when measuring the interfacial area density in dispersed flows.

In this paper a statistical analysis that generalizes the calculation of local interfacial variables in bubbly flows from data taken with a double-sensor intrusive probe is presented. The approach used herein relies on a statistical post-processing algorithm relating the probability distribution functions of the apparent (as measured by the probe) bubble velocity and chord length to the distribution of the actual variables. To develop this analysis, one followed a number of assumptions describing the multidimensional nature of the bubble displacement. It

has a general nature in the sense that the influence of the entrance angle on the bubble trajectory is accounted for. It is based on the pioneering works of Herringe and Davis (1976) and Kataoka et al. (1986), who first estimated the bubble size from intersected chords, and who first considered multidimensional effects in bubbly flows, respectively.

The main objective is to determine two fundamental statistical functions of actual quantities. Namely, the probability density function (PDF) of the actual (1) interfacial (or bubble) velocity and (2) bubble size. Coupled with the direct measurement of the void fraction and bubble frequency, some other local interfacial properties stem from these fundamental functions: interfacial area density, interface velocity fluctuation intensity and superficial gas velocities.

The paper is organized into four sections. The first section is the introduction. In Section 2 one deduces the relationships existing between the apparent and actual quantities, bubble (interface) velocity and bubble size, for both the isolated bubble and the swarm of bubbles. Section 2 ends describing the numerical algorithm that evaluates the distribution of actual variables from the analytical relationships and measured values. Section 3 presents the experimental apparatus, the probe, the threshold criteria to obtain the phase indicator function and the data acquisition system. In Section 4 the results are presented and compared with published data. Finally, the conclusions are drawn in Section 5.

2. Analysis

The relationship that exists between the apparent and actual interfacial variables of an isolated bubble that flows immersed in a liquid is the first subject of this analysis. These variables are the interface (or bubble) velocity and the bubble size. The apparent velocity, which is measured by the probe, does not necessarily equal the actual velocity. As a result, the chord length that is intersect by the probe does not necessarily match the actual one. The above mentioned relationships depend on the probe and bubble geometry and on the bubble trajectory regarding the probe axis. To calculate them one assumes that (1) the flow is stationary; (2) the bubbles are spherical; (3) the probe is aligned with the main flow direction and does not disturb the liquid phase; and (4) the intrusion of the probe neither alters the bubble trajectory nor distorts the gas–liquid interface.

In a further step, the analysis is extended from the single bubble to a swarm of gas bubbles dispersed in a liquid flow, characterizing a bubbly flow. The variables are now expressed as probability distribution functions. The actual and apparent probability functions may differ for several reasons: the flow is multidimensional and the bubble displaces along a spatial trajectory; the velocity fluctuation due to turbulence and/or the bubble–fluid interaction may cause, on the bubble trajectory, a misalignment angle — the so called *entrance angle* — regarding the probe axis (Kataoka et al., 1986). Coupled with this, one must consider the fact that the probe does not always intersect a bubble at its center. The statistical analysis presented herein, taking into account the reasoning above, establishes a procedure to estimate the actual probability functions of the bubble velocity and the intersected chord from the measured, or apparent, ones.

2.1. The single bubble: actual and apparent bubble velocity and size

Fig. 1 shows a sketch of the jth spherical bubble of diameter D_j touching the probe with an actual velocity V_{b_j}. The double-sensor probe is depicted as two dots, representing the front sensor, F (coincident with dot labeled A on the bubble surface, Fig. 1), and the rear sensor, R. They are separated from each other, and aligned along the zz' axis, which is coincident with the mean flow direction. The angle between the velocity V_{b_j} and the zz' axis is named the entrance angle, γ. The points where the sensors touch the bubble surface are represented by A and A' and refer, respectively, to the front and rear sensors. Two auxiliary variables, the polar, ξ, and conical, ϕ, angles, defining a spherical coordinate system, will be used. The angle ϕ is formed by V_{b_j} and n_j, the unit normal vector at A; ξ is the polar angle measured on a plane normal to V_{b_j}. The lines defined by the segments AR and $A'R$ are parallels with zz' and V_{b_j} having length ℓ and s_j, respectively.

Defining Δt_j as the time lapse the jth interface spends to travel between the sensors, the bubble actual velocity is expressed as follows:

$$V_{b_j} = \frac{s_j}{\Delta t_j} \tag{1}$$

The apparent velocity, V_{s_j}, as measured by the probe, is

$$V_{s_j} = \frac{\ell}{\Delta t_j}, \tag{2}$$

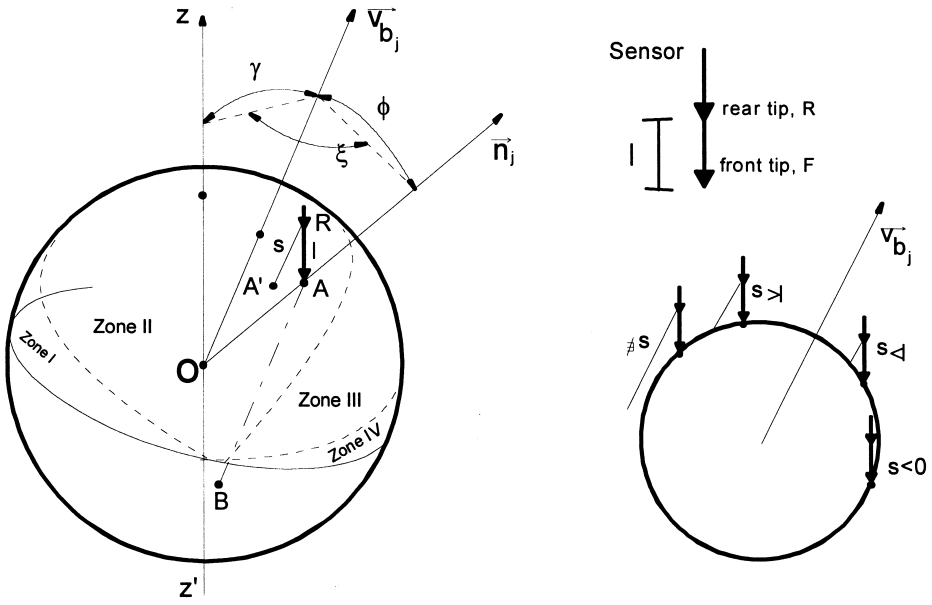

Fig. 1. Geometrical variables.

and depends strongly on the contact point A, as pointed out by Kataoka et al. (1986). Finally, the ratio between the apparent and the actual velocity is:

$$\frac{V_{s_j}}{V_{b_j}} = \frac{\ell}{s_j} \tag{3}$$

The dependence of the velocity ratio (3) on the contact point A is justified by geometrical arguments. The spherical bubble can be divided into two hemispheres by a plane whose normal is parallel with the bubble velocity, V_{b_j}. The upper hemisphere, shown in Fig. 1, can be divided again into four zones. Within each zone these variables behave as described below:

1. Zone I: If the contact point A is within this region, the front sensor touches the bubble, but not the rear sensor. Therefore, there is no apparent velocity;
2. Zone II: Due to the bubble radius on the locus of the contact point A, the distance ℓ is always shorter than s_j within this zone. Therefore, the actual velocity is greater than the apparent one;
3. Zone III: In this zone the distance ℓ is always greater than s_j, i.e., the opposite of zone II. Thus, the actual velocity is smaller than the apparent one;
4. Zone IV: The front sensor touches the bubble after the rear sensor. Hence, within this zone negative apparent velocities occur.

Referring again to Fig. 1, the front sensor pierces the bubble at point A, and leaves it at B. The segment AB defines the intercepted chord. Defining t_{F_j} as the residence time the jth bubble is in contact with the front sensor, the apparent and actual chord length, X_{s_j} and X_{s_j}, are:

$$X_{s_j} = t_{F_j} \cdot V_{s_j}, \tag{4}$$

$$X_{b_j} = t_{F_j} \cdot V_{b_j}. \tag{5}$$

Noticing that the actual chord length, X_{b_j}, is

$$X_{b_j} = D_j \cos(\phi_j), \tag{6}$$

the ratio between the apparent chord length and the bubble diameter:

$$\frac{X_{s_j}}{D_j} = \left(\frac{\ell}{s_j}\right) \cos(\phi_j). \tag{7}$$

The velocity and the chord ratios, defined by Eqs. (3) and (7), are given in terms of ℓ and s_j, which are distances pertaining to the probe and bubble geometry. If the bubble trajectory and the axis of the probe are parallel, one gets $\gamma = 0$ and $(\ell/s_j) = 1$. In the more general case of multidimensional flows with $\gamma \neq 0$, the velocity and chord ratio can be greater or less than unity, depending on the values that ℓ and s_j assume. In fact, (ℓ/s_j) depends on the value the angles ϕ, ξ, γ may take for the jth bubble:

$$\left(\frac{\ell}{s}\right)_j = \left[\frac{D_j}{\ell}\frac{\cos(\phi_j)}{2} + \cos(\gamma_j) - \left\{\left(\frac{D_j}{\ell}\frac{\cos(\phi_j)}{2}\right)^2 - \frac{D_j}{\ell}\sin(\gamma_j)\cos(\xi_j)\sin(\phi_j) - \sin^2(\gamma_j)\right\}^{1/2}\right]^{-1}. \tag{8}$$

If the bubble diameter is much larger than the lengthwise distance between sensors, $D \gg \ell$ the effect of the bubble surface curvature on the ratio (ℓ/s_j) is then negligible, and the contact surface can be approximated by a tangent plane on A. Therefore, for $(D/\ell) \gg 1$ the dependence of (ℓ/s_j) on D_j vanishes, and Eq. (8) simplifies to:

$$\left(\frac{\ell}{s_j}\right) \cong \left[\cos(\gamma_j) + \sin(\gamma_j)\cos(\xi_j)\tan(\phi_j)\right]^{-1}. \tag{9}$$

The ratio (ℓ/s_j), given exactly by Eq. (8), or in an approximate form by Eq. (9), is a fundamental geometrical quantity. The velocity and chord length ratios stem directly from (ℓ/s_j) and can be specified in terms of the angles ϕ, ξ, γ, substituting Eq. (8) in Eq. (3) and Eq. (8) in Eq. (7), or Eq. (9) in Eq. (3) and Eq. (9) in Eq. (7) if $(D/\ell) \gg 1$ applies.

2.2. The statistical analysis for a bubbly flow

If one considers a swarm of bubbles, the probability of (ℓ/s) within $d(\ell/s)$ is:

$$p\left(\frac{\ell}{s}\right)d\left(\frac{\ell}{s}\right) = \int_{\phi,\,\xi,\,\gamma,\,D} p(D,\phi,\xi,\gamma)\,d(D)\,d(\xi)\,\mathrm{d}(\gamma). \tag{10}$$

where D, ϕ, ξ and γ define a multidimensional region where (ℓ/s) occurs and $p(\ell/s)$ is the probability density function of (ℓ/s).

In Eq. (10), the geometrical variables D, ϕ, ξ, γ and s, no longer refer to the jth bubble, but are random variables. Furthermore, considering that the probe touches the bubble at points randomly distributed over its surface, and assuming that the events of D, ϕ,ξ,γ are statistically independent, Eq. (10) can be re-written as:

$$p\left(\frac{\ell}{s}\right)d\left(\frac{\ell}{s}\right) = \int_{\phi,\,\xi,\,\gamma,\,D} p(D)p(\phi)p(\xi)p(\gamma)\,d(D)\,d(\phi)\,d(\xi)\,d(\gamma). \tag{11}$$

If one now extends the geometrical relationships that apply for a single bubble, Eqs. (3) and (7), to the swarm of bubbles that characterizes a bubbly flow, the PDFs $p(V_s/V_b)$ and $p(X_s/D)$ are:

$$p\left(\frac{V_s}{V_b}\right) = p\left(\frac{\ell}{s}\right), \tag{12}$$

$$p\left(\frac{X_s}{D}\right) = p\left(\frac{\ell\cos\phi}{s}\right). \tag{13}$$

2.3. Analytical expressions for the velocity and chord ratio distributions

The probability density function $p(\ell/s)$ becomes fully established when one constitutes the PDFs $p(D)$, $p(\phi)$, $p(\xi)$ and $p(\gamma)$. These statistical functions derive from the bubble and probe geometry and from assumptions concerning the characteristics of the flow field as follows:

- The PDF $p(D)$ may depend on several factors: gas and liquid flow rates, fluid properties, pipe diameter and characteristics of the gas–liquid mixer. Unfortunately, no assumption related to this function can be made in advance. Even though one stresses that this dependence shall vanish if the bubble diameter is much greater than the lengthwise sensor spacing, $(D/\ell) \gg 1$, the approximation of Eq. (9) holds. In view of these difficulties, no contribution of $p(D)$ is considered beforehand when $p(\ell/s)$, Eq. (11), is evaluated. Actually, the method itself is a proposition to evaluate it. The implications of this bold assumption are verified when the final results are obtained and checked.
- For a spherical bubble, the probability density function $p(\phi)$ is given by Herringe and Davis (1976):

$$p(\phi) = \sin(2\phi), \quad 0 \le \phi \le \frac{\pi}{2}. \tag{14}$$

- The polar angle ξ may take any value between 0 and 2π with equal probability. Therefore,

$$p(\xi) = \frac{1}{2\pi}, \quad 0 \le \xi \le 2\pi. \tag{15}$$

- To constitute the PDF $p(\gamma)$, one postulates that the entrance angle γ is settled by some flow characteristics: the void fraction, the bubble shape, the velocity field and the flow pattern. When the flow pattern is either the "laminar bubbly flow", typical of low void fraction, small and spherical bubbles, or the "churn-turbulent bubbly flow", appearing at higher void fractions (Ishii, 1975), one expects a uniform distribution of the entrance angle. Under these circumstances, assuming that γ is uniformly distributed within a solid angle γ_0, its PDF yields:

$$p(\gamma) = \frac{\sin\gamma}{1 - \cos\gamma_0}, \quad 0 \le \gamma \le \gamma_0. \tag{16}$$

Following Kataoka et al. (1986), and assuming that the bubble velocity fluctuation is isotropic, one can relate the limiting angle γ_0 to the axial component of the bubble velocity, V_{bz}, by means of its variance and mean value,

$$\gamma_0 \cong \sqrt{\frac{4\left(\sigma_{V_{bz}}/\bar{V}_{bz}\right)^2}{1 + 3\left(\sigma_{V_{bz}}/\bar{V}_{bz}\right)^2}}, \tag{17}$$

Knowing that $V_{bz} = V_b \cos\gamma$, the ratio $(\sigma_{V_{bz}}/\bar{V}_{bz})^2$ can be expressed as:

$$\left[\left(\frac{\sigma_{V_{bz}}}{\bar{V}_{bz}}\right)^2 + 1\right] = \left[\left(\frac{\sigma_{V_b}}{\bar{V}_b}\right)^2 + 1\right] \frac{\overline{\cos^2\gamma}}{(\overline{\cos\gamma})^2}. \tag{18}$$

Substituting Eqs. (14)–(16) in Eq. (11), the probability function for (ℓ/s) is found as:

$$p\left(\frac{\ell}{s}\right)d\left(\frac{\ell}{s}\right) = \int \frac{\sin 2\phi \sin \gamma}{2\pi(1-\cos\gamma_0)}\,\mathrm{d}(\phi)\,\mathrm{d}(\xi)\,\mathrm{d}(\gamma), \tag{19}$$

When the bubbles grow above a certain critical size, the flow pattern is called the "distorted bubble regime" (Ishii, 1977). In this case, a constant entrance angle is likely to occur: the bubbles displace along a helical path, usually referred to as a "zigzag path of distorted bubbles," as viewed on a plane (Saffman, 1956). Considering the occurrence of a constant entrance angle, Eq. (19) is further simplified to:

$$p\left(\frac{\ell}{s}\right)d\left(\frac{\ell}{s}\right) = \int \frac{\sin 2\phi}{2\pi}\,\mathrm{d}(\phi)\,\mathrm{d}(\xi). \tag{20}$$

An explicit expression for $p(\ell/s)$ could be cast if the variables ϕ, ξ, γ, appearing in Eq. (8) or Eq. (9), could be expressed in terms of the ratio (ℓ/s). The same applies to $p(V_s/V_b)$ and $p(X_s/D)$ as seen in Eqs. (12) and (13). Since such transformation was not possible to achieve, the PDFs $p(\ell/s)$, $p(V_s/V_b)$ and $p(X_s/D)$ were numerically evaluated. The results are shown in succession.

Fig. 2 depicts the velocity ratio PDF, $p(V_s/V_b)$, for γ uniformly distributed within a solid angle γ_0, and $(D/\ell) = 1.5$. The three curves in the plot refer to different values of γ_0, 10°, 20° and 30°. One observes in Fig. 2 that as γ_0 increases from 10° to 30°, the expected average value and the standard deviation shift, respectively, from 1.019 to 1.130, and from 0.1139 to 0.3193. As the limiting angle γ_0 reduces, $p(V_s/V_b)$ becomes sharper, increasing the probability of measuring velocities closer to the actual bubble velocity.

The curves in Fig. 3 are the PDFs of the chord ratio, $p(X_s/D)$. Again, the three curves refer to $\gamma_0 = 10°$, 20° and 30° and $(D/\ell) = 1.5$. Notice that, if the entrance angle is finite, the probe

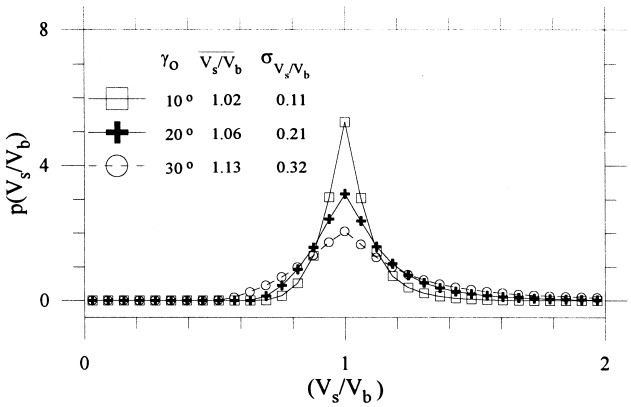

Fig. 2. PDF of the velocity ratio, $p(V_s/V_b)$, for $(D/\ell) = 1.5$ and γ uniformly distributed within a solid angle of 10°, 20° and 30°.

may measure apparent chord lengths even larger than the bubble diameter. The larger the limiting angle γ_0 is, the higher is the chance of measuring apparent chords larger than D. The increase from 10° to 30° does not translate into major changes in the $p(X_s/D)$. In fact, the averaged value of the chord length ratio, shifts only from 0.71 to 0.78 when γ_0 increases from 10° to 30°.

Figs. 4 and 5 show the influence of the lengthwise distance between sensors upon $p(V_s/V_b)$ and $p(X_s/D)$, yet for a uniform distribution of γ, with $\gamma_0 = 20°$ The open circle symbol refers to the approximation of Eq. (9): $(D/\ell) \gg 1$ and $p(\ell/s)$ has no dependence on the bubble diameter probability function. The solid circle symbol refers to $(D/\ell) = 0.8$, a typical value, for example, in Serizawa et al. (1975a); the cross symbol applies for $(D/\ell) = 1.5$. Most of the works reporting measurement of bubble velocity and diameter do not consider the bubble surface curvature effect, in other words, they assume $(D/\ell) \gg 1$. As the ratio (D/ℓ) increases from 0.8 to infinity, for example, there is only a minimum change in the mean velocity ratio, (V_s/V_b), from 1.048 to 1.061. However, the standard deviation of the velocity ratio increases from 0.1139 to 0.3193. The analysis is quite similar for mean chord ratio, (X_s/D); its mean value varies from 0.7349 to 0.7289, and the standard deviation, from 0.1968 to 0.3298.

The probability functions $p(V_s/V_b)$ and $p(X_s/D)$ for a constant entrance angle are shown in Figs. 6 and 7. The three curves correspond to $\gamma = 10°$, 20° and 30°, and apply to $(D/\ell) = 1.5$. As one would expect, the probability of measuring velocities that fall away from the actual bubble velocity increases if the results are compared with the cases for γ uniformly distributed. The PDF $p(X_s/D)$ spreads out even more in Fig. 6 compared with Fig. 3, which applies for a uniform distribution of $\gamma = 20°$. For $\gamma = 20°$ and $\gamma = 30°$, the curves have a significant number of apparent chord lengths that are larger than the bubble diameter.

The influence of the characteristics of the entrance angle and the magnitude of (D/ℓ) on the PDFs $p(V_s/V_b)$ and $p(X_s/D)$ are fully explored in Dias (1998).

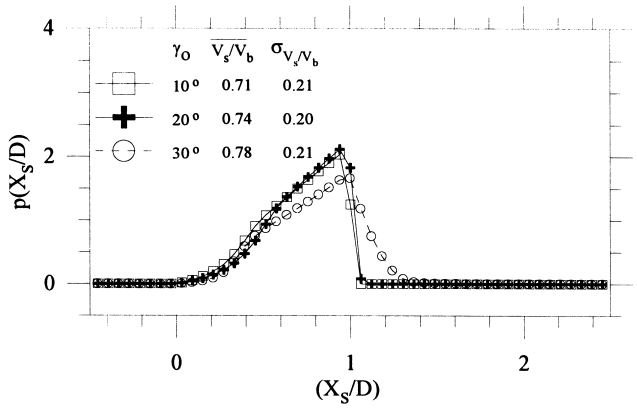

Fig. 3. PDF of the chord ratio, $p(X_s/D)$, for $(D/\ell) = 1.5$ and γ uniformly distributed within a solid angle of 10°, 20° and 30°.

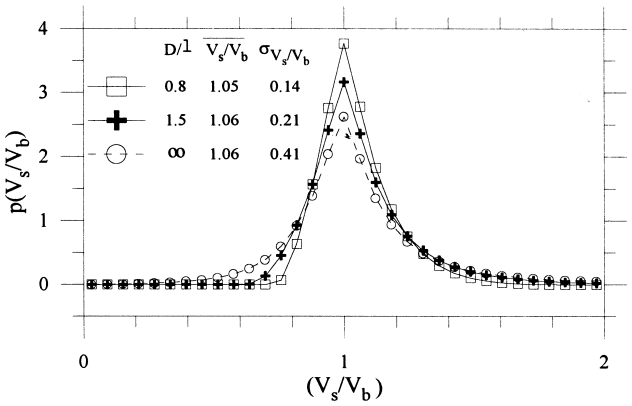

Fig. 4. PDF of the velocity ratio, $p(V_s/V_b)$, for γ uniformly distributed within a solid angle of 20° and $(D/\ell) = 0.8$, 1.5 and ∞.

2.4. Calculating the distribution of the actual velocity and chord length

Consider now an idealized bubbly flow: the mixture has bubbles of uniform diameter displacing at constant velocity along the one-directional trajectory parallel to the probe axis. The apparent velocity, as measured by the probe, would show up as a constant value. The chord length, however, would spread around an average value, as a result of the randomness of the position where the sensor touches the bubble, which is related to the angle ϕ. This simple case illustrates that the non-deterministic nature of the measuring method is due not only to the flow fluctuations or the multidimensional bubble trajectories, but also to the randomness of the contact point.

In a less restrictive flow, the approach requires the disclosure of the actual variables —

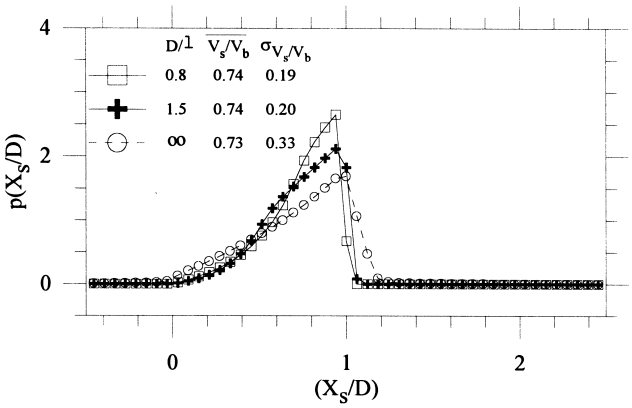

Fig. 5. PDF of the chord ratio, $p(X_{s/D})$, for γ uniformly distributed within a solid angle of 20° and $(D/\ell) = 0.8$, 1.5 and ∞.

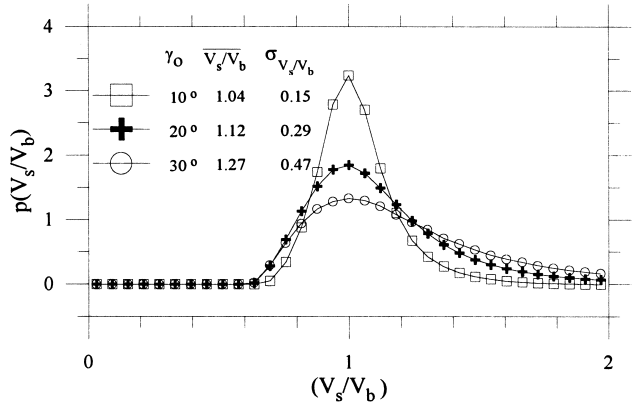

Fig. 6. PDF of the velocity ratio, $p(V_s/V_b)$, for $(D/\ell) = 1.5$ and a constant entrance angle, γ, of 10°, 20° and 30°.

bubble velocity and chord length distribution — from the apparent ones. The PDFs $p(V_s/V_b)$ and $p(X_s/D)$ arise from geometrical relationships concerning the bubble shape and the probe dimension and, moreover, upon the entrance angle. Then, one postulates they become independent or, at least, have a weak dependence on $p(V_b)$ and $p(X_b)$. Hence, the probability, $p(V_s)d(V_s)$, can be written as the joint distribution of the velocity ratio and the actual velocity:

$$p(V_s)d(V_s) = \int_{-\infty}^{+\infty} p(V_s/V_b)d(V_s/V_b)p(V_b)d(V_b) \tag{21}$$

Similarly for the chord length,

$$p(X_s)d(X_s) = \int_{-\infty}^{+\infty} p(X_s/D)d(X_s/D)p(D)d(D). \tag{22}$$

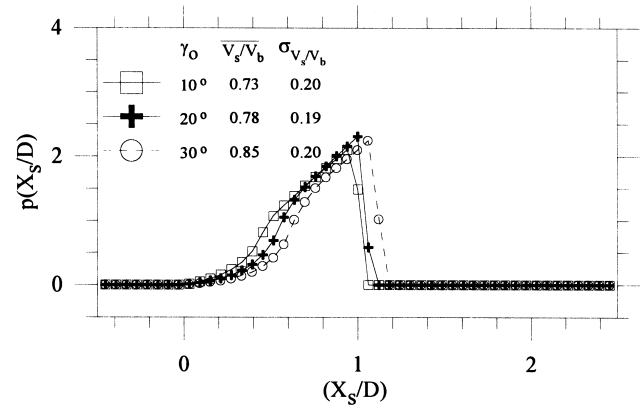

Fig. 7. PDF of the chord ratio, $p(X_s/D)$, for $(D/\ell) = 1.5$ and a constant entrance angle, γ, of 10°, 20° and 30°.

The generality of these two equations derives from the fact that $p(V_s)$ and $p(X_s)$ are not defined a priori.

Defining the first and the second statistical moments of a random variable Y as:

$$\bar{Y} = \int_Y p(Y) \cdot Y \, dY, \qquad \overline{Y^2} = \int_Y p(Y) \cdot Y^2 \, dY, \tag{23}$$

one can establish, from Eqs. (21) and (22), the relationship between the first and second statistical moments of the velocities and of the intersected chord length as:

$$\overline{V_s} = \overline{\left(\frac{V_s}{V_b}\right)}\overline{V_b}, \qquad \overline{V_s^2} = \overline{\left(\frac{V_s}{V_b}\right)^2}\overline{V_b^2}, \tag{24}$$

$$\bar{X}_s = \left(\frac{\bar{X}_s}{D}\right)\bar{D}, \qquad \bar{X}_s^2 = \left(\frac{\bar{X}_s}{D}\right)^2 \overline{D^2}. \tag{25}$$

Eqs. (24) and (25) express the local mean velocity and the chord length in terms of their respective distributions. Similar to Eqs. (21) and (22), the difference between the actual bubble mean velocity, $\bar{V}_b$, and the apparent one, $\bar{V}_s$, depends on the mean value of the $p(V_s/V_b)$; the same reasoning applies to the actual mean bubble diameter $\bar{D}$ and the measured mean chord length, $\bar{X}_s$. Looking at the difference between apparent and actual mean values, Figs. 2 and 5 show that the mean value of $p(V_s/V_b)$ may attain values up to 1.27. Conversely, the mean value of $p(X_s/D)$ is invariably less than one, as shown in Figs. 3, 4 and 6, and can be as low as 0.70. The variances of the actual bubble velocity and diameter are defined as:

$$\sigma_{V_b}^2 = \overline{(V_b^2)} - (\bar{V}_b)^2 \quad \text{and} \quad \sigma_D^2 = \overline{(D^2)} - (\bar{D})^2. \tag{26}$$

Using Eqs. (24) and (25), the mean and the variance of the actual distributions are determined. On the other hand, to know the whole frequency spectrum of each variable, it is necessary to determine the PDFs from Eqs. (21) and (22). The analytical functions $p(\ell/s)$ and $p(\ell \cos\phi/s)$ and their measured counterparts, $p(V_s)$ and $p(X_s)$, will form a system of equations whose solutions are the actual bubble velocity and size distribution, $p(V_b)$, and $p(D)$. The integral equations, Eqs. (21) and (22), are solved numerically, approximating them by a summation of discrete terms, as indicated by Eqs. (27) and (28):

$$p(V_{s_i})\Delta(V_{s_i}) = \sum_{k=1}^{M} p(V_{s_i}/V_{b_k})\Delta(V_{s_i}/V_{b_k})p(V_{b_k}), \quad i = 1, \ldots, N \tag{27}$$

$$p(X_{s_i})\Delta(X_{s_i}) = \sum_{k=1}^{M} p(X_{s_i}/D_k)\Delta(X_{s_i}/D_k)p(D_k)\Delta(D_k), \quad i = 1, \ldots, N \tag{28}$$

where N and M are the number of classes of V_s and V_b in Eq. (27), or the number of classes of X_s and D in Eq. (28), respectively. $\Delta(V_{s_i})$, $\Delta(V_{b_k})$ and $\Delta(V_{s_i}/V_{b_k})$ represent the class intervals of

$p(V_s)$, $p(V_b)$ and $p(V_s/V_b)$ in Eq. (27). Similarly, $\Delta(X_{s_i})$, $\Delta(D_k)$ and $\Delta(X_{s_i}/D_k)$ represent the class intervals of $p(X_s)$, $p(D)$ and $p(X_s/D)$ in Eq. (28).

The experimental values of V_s or X_s define intervals, which bound the expected values of V_b and D, respectively. Without loss of generality, one can specify the actual variables, V_b and D, to vary within the same range as the apparent variables, V_s and X_s. Furthermore, to simplify the evaluation, one can assume that the number of classes is equal, i.e., $N = M$. These assumptions lead to:

$$V_{s]\min} \le V_b \le V_{s]\max}, \quad X_{s]\min} \le D \le X_{s]\max}, \quad \Delta(V_{s_i}) = \Delta(V_{b_k}) \quad \text{and} \quad \Delta(X_{s_i}) = \Delta(D_k).$$

Eqs. (27) and (28) are generically written in a matrix form as:

$$\begin{bmatrix} C_{1,1} & C_{1,2} & \cdots & C_{1,N} \\ C_{2,1} & C_{2,2} & \cdots & C_{2,N} \\ \vdots & \vdots & \vdots & \vdots \\ C_{N,1} & C_{N,2} & \cdots & C_{N,N} \end{bmatrix} \cdot \begin{bmatrix} I_1 \\ I_2 \\ \vdots \\ I_N \end{bmatrix} = \begin{bmatrix} O_1 \\ O_2 \\ \vdots \\ O_N \end{bmatrix}. \tag{29}$$

The coefficient $C_{i,k}$ is the product of $p(V_s/V_b)$, or $p(X_s/D)$, by its respective class interval; I_i is the actual probability, $p(V_b)d(V_b)$ or $p(D)d(D)$, and O_i is the apparent probability, $p(V_s)d(V_s)$ or $p(X_s)d(X_s)$, measured by the probe. For convenience, Table 1 exhibits the forms that $C_{i,k}$, I_k and O_i may take when used to represent Eq. (27) or Eq. (28).

Rather than getting the unknowns directly from Eq. (29), the linear system is solved as an optimization problem, requiring a minimum value for the residual R,

$$R = \sqrt{\frac{\sum_{i=1}^{N}\left(O_i - \sum_{i=1}^{N} C_{i,k} I_k\right)^2}{N}}, \tag{30}$$

subjected to the following constraints:

$$I_k \ge 0 \quad \text{and} \quad \sum_{i=1}^{N} I_k = 1. \tag{31}$$

The optimization was an effective tool to estimate $p(V_b)$ and $p(D)$. In some cases, a direct solution of Eq. (25) gave inconsistent results, as a negative value for $p(V_{b_j})\Delta(V_{b_j})$. One imputes

Table 1
Coefficients in Eq. (29)

For use in	$C_{i,k}$	I_k	O_i
Eq. (23)	$p(V_{s_i}/V_{b_k})\Delta(V_{s_i}/V_{b_k})$	$(V_{b_k})\Delta(V_{b_k})$	$p(V_{s_i})\Delta(V_{s_i})$
Eq. (24)	$p(X_{s_i}/D_k)\Delta(X_{s_i}/D_k)$	$p(D_k)\Delta(D_k)$	$p(X_{s_i})\Delta(X_{b_i})$

this direct solution deficiency to the fact that the apparent distribution, as measured by the probe, is only a sub-set of all possible values that the variables may take.

The numerical routine was implemented as a FORTRAN language. It runs in a PC-AT driven by a Pentium 100 MHz processor in 30 s, when the number of classes is $N = 60$, and the residual is less than 0.001.

3. Experimental technique

3.1. Experimental apparatus

To verify the method an experimental apparatus has been set up, Fig. 8. The test section consists of a 52 mm ID, clear, vertical, Plexiglas straight pipe, 50 diameters long. Its verticality was carefully verified. Ordinary tap water and air were the working fluids. The water was fed by a stainless steel centrifugal pump. The air was supplied by a large tank, 1.5 m^3, maintained at 8 bar. Two orifice plates, both with an accuracy within 2%, were used to measure the air and water flow rate, respectively. The air orifice plate was calibrated against a laminar element, while the liquid orifice suffered a primary calibration. The liquid and gas superficial velocities applied during the tests were up to 100 and 15 cm/s, respectively.

The air–water mixing chamber locates at the lower end of the vertical pipe. The mixing process develops through an adjustable annular space formed by the chamber wall and a cylindrical porous media. A fairly uniform mixing and quick development of an upward bubbly flow is achieved injecting the air through the porous media while the water is flowing through the annular space. The measuring section is 40 diameters upstream the air–liquid

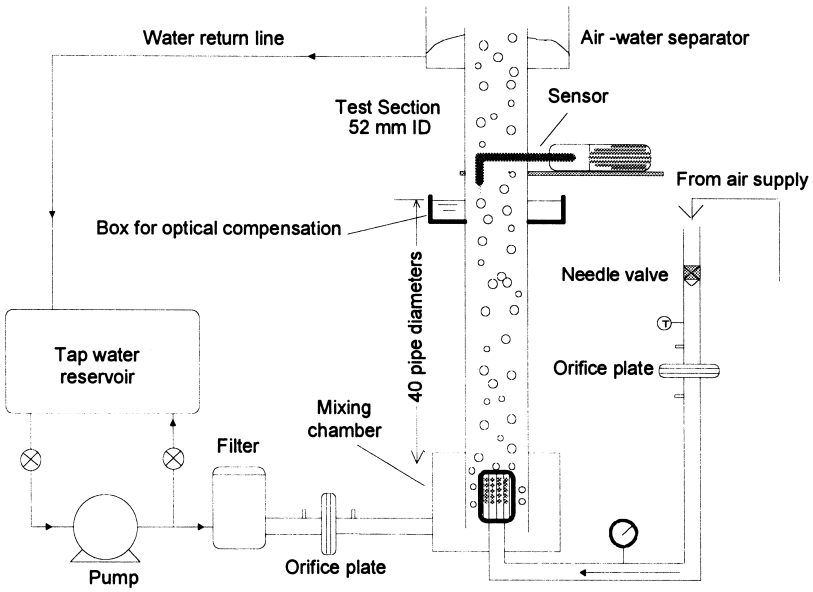

Fig. 8. Schematics of the experimental apparatus.

mixer. To allow photographic records, this section is surrounded by a Plexiglas square box. The box, filled with water, compensates for optical distortions introduced by the pipe curvature. The probe enters the test section through a side hole 2 mm in diameter. A radial displacing mechanism, driven by a micrometer, supports it. Downstream the test section, the mixture discharges into a separation tank. The water flows back to the reservoir by gravity, while the air is discharged into the atmosphere.

The double-sensor probe detects the change in the electrical resistance, in the medium surrounding the electrodes — the tip of the probe and its body. An electrical probe was chosen due to the relatively simple and inexpensive electronic signal conditioning circuit required to drive it and also, on the positive results for conducting liquids presented in the literature. The material of the probe and its geometrical dimensions are sketched in Fig. 9. The twin sensors are made of exposed tips, 120 μm in diameter, of an otherwise electrically insulated copper wire. The wires go through a stainless steel hypodermic needle of 700 μm OD. The needle gives structural support for the wires and acts a return electrode. The needle is attached to the micrometer, which transverses the probe across the pipe radius. The micrometer positions the probe within ± 0.02 mm. At the other end there are the exposed tips, preceded by a 90° elbow bend, which is at 30 needle diameters before the tips. The wires, insulated with varnish and encapsulated by the needle, are placed side by side with a silicon resin used for sealing and bonding. The lengthwise spacing between the front and rear sensors is 2000 ± 50 μm, and the exposed tip area is roughly the wire cross section area, 11000 μm^2.

3.2. Data acquisition system and phase indicator function

The two sensors work independently as phase indicators. The output voltage of the two channels signal conditioner fluctuates between a high and low value. The circuit is open (3.0 V) when air surrounds the tip and is closed (0 V) when water covers it. This choice of voltage polarization proved to be efficient in reducing undesirable drift due to electrochemical phenomena. The twin signal is sampled at 50 kHz per channel during a period of 1000 s by a

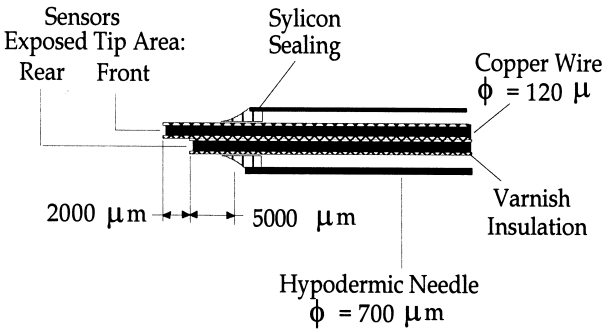

Fig. 9. Electrical probe assembly.

National Instruments® AT-MIO16, a 12 bits data acquisition board, driven by a 486 PC computer.

A typical sample of the raw signal for a bubble that hits first the front sensor and then the rear sensor, is shown in Fig. 10. This signal appears in terms of the percentage of the voltage span S, defined as:

$$S = 100\left(\frac{V-L}{H-L}\right), \tag{32}$$

where V, H and L are the instantaneous voltage, and the highest and the lowest levels, respectively. As observed in Fig. 10, the change of voltage shows a delay when the sensor penetrates the bubble (low to high). This change is almost instantaneous when the bubble leaves the tip. This is attributed to the hydrodynamics of the interface puncture process: before the sensor penetrates the bubble some liquid has to be drained and the force due to the interfacial tension has to be overcome. The interface deforms, the liquid flow field at that point alters, the bubble velocity changes and even some deviation in the bubble trajectory may occur. Cartellier and Achard (1991) presented a very comprehensive discussion in this regard.

The raw voltage data interpretation requires the setting of a threshold voltage, V_T. The threshold is used as a triggering criterion to identify the phases, transforming the original signal in a train of squared waves, known as the phase indicator function, see Fig. 10. The phase indicator function, $N_G(r, t)$ depends on the probe radial position, r, as well as on the time interval, and is defined as:

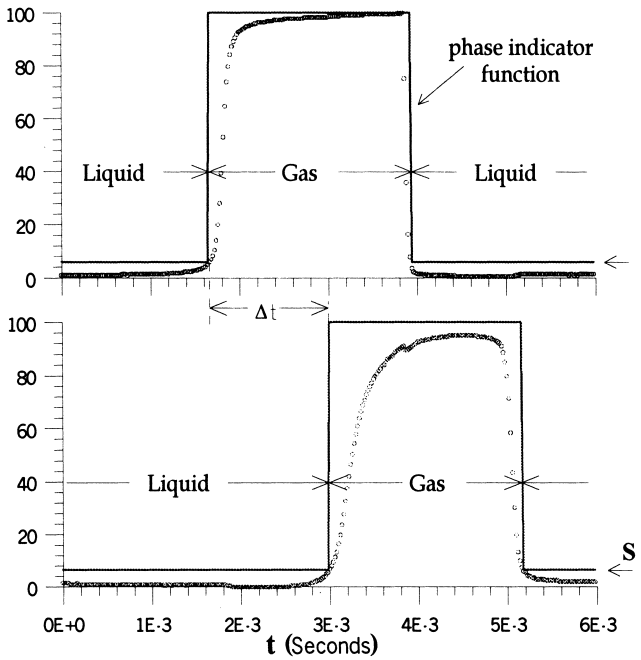

Fig. 10. Typical sample of the raw voltage signal and phase indicator function for the front and rear sensors.

$$N_G(r, t) = \begin{cases} 1, & \text{when there is gas at position } r \text{ in time } t \\ 0, & \text{when there is liquid at position } r \text{ in time } t. \end{cases} \tag{33}$$

Using the definition of the phase indicator function and designating by T the sampling period, one gets three other important local interfacial properties over the pipe radial position, r: the void fraction, $\varepsilon(r)$, bubble frequency, $f_b(r)$, and the mean sensor residence time inside the bubble, $\bar{t}(r)$;

$$\varepsilon(r) = \frac{1}{T}\int_{t=0}^{t=T} N_G(r, t)\, dt, \tag{34}$$

$$f_b(r) = \frac{1}{T}\int_T \frac{1}{2}\left|\frac{d}{dt}N_G(r, t)\right| dt, \tag{35}$$

$$\bar{t}(r) = \frac{\varepsilon(r)}{f_b(r)}. \tag{36}$$

3.3. Threshold level setting

Unfortunately, there is no definite agreement on the literature regarding the setting of a threshold level. Usually it stays within 10 to 50% of the span, depending on the above mentioned puncture process, under the influence of the fluids physical properties, flow velocities, probe dimensions, and on the response characteristics of the signal conditioner.

The first step toward the threshold level setting is to define the voltage span levels, H and L, which appeared in Eq. (32). This normalization is necessary since the raw signal can include undesirable base noise or undershoot or overshoot behavior, depending on how the signal conditioner responds to the phase change. For the present case, there is some base noise only when the signal is low (i.e., the tip of the probe is immersed in liquid); undershoot or overshoot signal behavior were minimized after carefully fine turning the signal conditioner, which meant an adjustment of the resistance in the reference bridge.

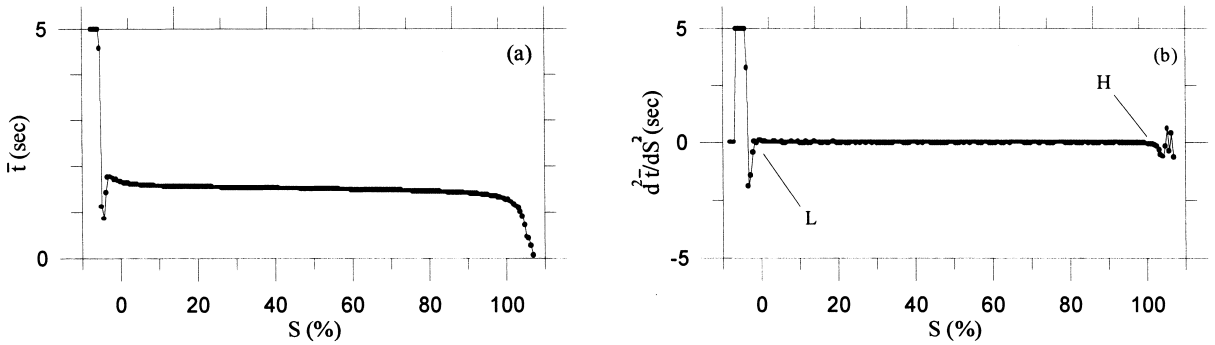

Fig. 11. Mean residence time (a) and its second derivative (b) vs. the relative threshold level.

The Fig. 11(a) shows the mean residence time of front sensor, i.e., the period the sensor stays inside the bubble, Eq. (36), plotted as a function of the relative threshold level. This threshold level can vary from 0 to 3 V, corresponding to the minimum and maximum voltages attained by the circuit. To get rid of the undesirable background noise and overshoot or undershoot behavior induced by the electronic circuit, one proposes to re-scale, from 0 to 100%, the range between the absolute L and H voltages which sets the range where mean residence time behaves as a slow varying function. When the threshold level is low, background oscillations appear as if small bubbles were hitting the probe. This changes the mean residence time, which varies suddenly and then increases sharply. When the relative threshold is set to a very high level, the mean residence time falls quickly, as the interpretation is that the liquid involves the probe most of the time. In between, there is a range where the mean residence time behaves as a slow varying function. The new signal voltage span is then defined taking the second derivative of the mean residence time in relation to the threshold level (Fig. 11b), and choosing L and H as the limits where the second derivative is very close to zero.

After defining the voltage span, another question arises: are the threshold level for the front and rear sensors independent? In fact, one may argue that the front sensor, due to probe intrusion, may cause a deviation on the bubble trajectory, lowering the void fraction and the bubble frequency measured by the rear sensor. Conversely, one may assume that the front sensor does not cause any trajectory deviation and just slows down the bubble. The rear sensor will indicate a higher void fraction, besides measuring the same bubble frequency as the front sensor. This question was dealt with in a vast number of experiments, depicted in Fig. 12. Fig. 12(a) shows a comparison between the void fraction, as measured by the front and rear sensors. In Fig. 12(b) the same comparison holds for the bubble frequency. The threshold is

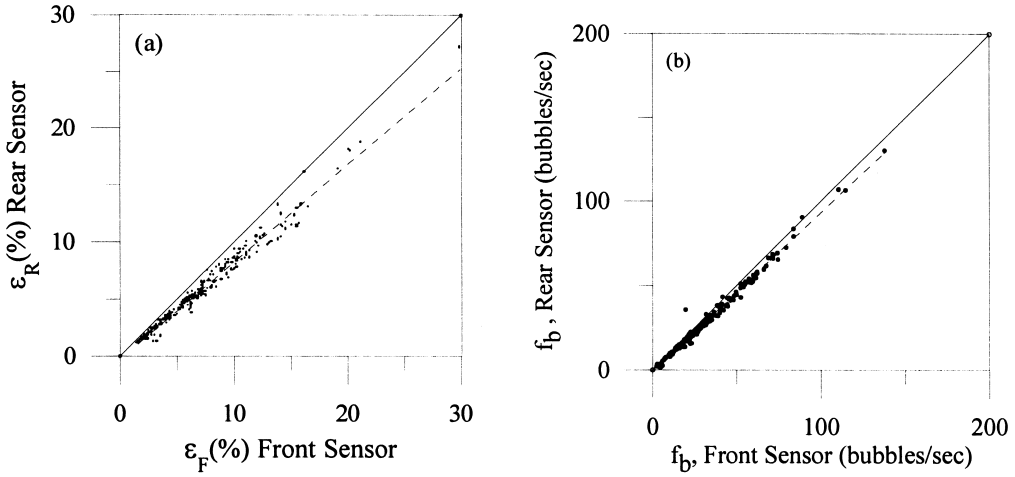

Fig. 12. Void fraction (a) and bubble frequency (b) for a constant threshold level: comparison between the measurements delivered by the front and rear sensors.

the same in both Fig. 12(a) and (b), where the dashed line is the least square linear fit for the experimental data; the solid line equates the front and rear sensor measurements.

The situation depicted in Fig. 12(a) and (b) is typical in all the experimental runs and does not depend on the threshold if the same level is set for both signals. One notes in Fig. 12(a) that the front sensor measures a systematically higher void fraction. In a less pronounced way, the same holds when one compares the bubble frequency. The deviation between the front and rear sensor measurement is lower for the frequency when compared with the deviation in void fraction. If the great majority of bubbles hitting the front sensor also hits the rear sensor, the bubble trajectory deviation is a less pronounced effect than the interface deformation or the change in the bubble velocity. To compensate these effects, the threshold for the rear sensor signal shall be adjusted to a lower level, so that it will deliver the same void fraction, $\varepsilon_R(r)$, as the front sensor, $\varepsilon_F(r)$:

$$\varepsilon_F(r) = \varepsilon_R(r). \tag{37}$$

Due to the lower sensitivity of the rear sensor Eq. (37) could not be enforced for less than 10% of the 180 data points collected from eighteen runs. For these particular cases the threshold for the rear sensor was lowered to 0% and Eq. (37) could not be satisfied. In those cases one adjusted the rear sensor threshold value to 0% of the span.

One may now continue looking for a procedure to set the threshold level for the front sensor. In fact, the values for the threshold level applied to the front sensor comes out from a calibration. To calibrate the probe one takes the product of the local bubble velocity times the void fraction, as measured by the probe, and integrates it over the pipe cross section to evaluate the average gas superficial velocity, $\langle J_G^V \rangle$:

$$\langle J_G^V \rangle = \frac{\int_0^R 2\pi r \varepsilon(r) V_{bz}(r)\, dr}{\int_0^R 2\pi r\, dr}, \tag{38}$$

The symbol $\langle\ \rangle$ denotes cross section area-averaged values and R is the pipe radius. This averaged value of the gas superficial velocity is then compared with the superficial gas velocity obtained by the volumetric measurement, $\langle J_G \rangle$. Referring the Q_G as the volumetric gas flow rate, if A is the pipe cross sectional area the gas superficial velocity is:

$$\langle J_G \rangle = \frac{Q_G}{A}. \tag{39}$$

Ideally, the calibration should be a recurrence procedure, since the threshold setting determines the quantities $\varepsilon(r)$ and $\bar{V}_{bz}(r)$, and one looks for a threshold level that gives a lower average deviation between the values calculated by Eqs. (38) and (39). Appropriate values for the threshold level are shown in Table 2 for distinct liquid superficial averaged velocities, $\langle J_L \rangle$. These results are independent of the gas flow rate. There is a clear tendency for decreasing threshold settings as the liquid superficial velocity increases. This behavior can be, in part, attributed to the bubble piercing process. Negative values indicate that, for the highest liquid

superficial velocities, a no deviation condition can exist for a threshold set between the two discrete values of 5 and 10%.

3.4. Classification of bubble signals

After setting the threshold and discriminating the phases, the next step is to identify the signals delivered by the probe when a bubble is pierced by the front and rear sensors. Due to the possibility of intercepting bubbles whose trajectories are not aligned with the probe axis, the classification criterion becomes broader than the ones commonly used. The signals are classified into seven cases, shown in Fig. 13. As indicated, Δt_j is the time interval spent by the bubble to travel between sensors and is used in Eq. (2) to calculate the apparent bubble velocity, and T_F and t_R are residence time.

Case 1 shows a typical signal: the bubble hits first the front sensor and then the rear sensor. In this situation, $\Delta t_j \leq t_{F_j}$. Signals that appear as Cases 2 and 3 do not count for computing the bubble velocity as the method itself is not provided with the distance s (defined in Fig. 1). Case 4 is similar to case 1, except that $t_{F_j} > t_{F_j}$ and $\Delta t_j \leq t_{F_j}$ (the chord pierced by the front sensor is larger than the one pierced by the rear sensor). Cases 5 and 6 arise when the bubble hits the rear sensor and then the front sensor. Finally, in Case 7 the signals do not overlap themselves and are spaced by Δt_j. To account for the events appearing in Case 7, one calculates the ratio $(\ell/\Delta t_j)$ as a way of establishing a minimum velocity and to find out if the same bubble has hit the front and rear sensor. If $(\ell/\Delta t_j) > 25$ cm/s, the signals are considered to compute the bubble velocity; otherwise, the signals are classified as Case 2 or Case 3 above. This criterion is similar to the waiting time introduced by Leung et al. (1995).

3.5. Evaluation procedures for the PDFs

The procedures to evaluate the bubble velocity and bubble diameter actual PDFs are summarized in the flow chart of Fig. 14. The steps (1), (2), (3) and (4) are concerned with signal acquisition, threshold level setting and the transformation process that changes the voltage time series in a normalized signal (squared wave) ranging from 0 to 100% of the voltage span, as indicated in Section 3.3. The steps (5) to (11) comprise two control loops that, interactively, find the solution for the bubble averaged diameter and γ_0. In step (12) the actual

Table 2
Threshold level × averaged liquid superficial velocity

J_L (cm/s)	Threshold level (%)	Deviation (%) $100(\langle J_G^V \rangle - \langle J_G \rangle)/\langle J_G \rangle$
0	20	+8.5
26	15	+5.9
51	10	+2.9
76	5	−0.9
103	5	−0.9

PDFs of the gas velocity and bubble diameter are evaluated at every radial position by solving Eqs. (29) and (30).

Step (3) to (11) form the core of the algorithm. Step (3) applies a threshold value to normalize the signal delivered by the front sensor. This value is set in accordance with Table 2, within the range 5 to 20% of the voltage span, remaining the same for the whole set of data points spanning across the pipe radius. Step (4) is a reading routine that generates the normalized signal (0 to 100%) from every radial position along the pipe radius. Once the data belonging to the ith pipe radial position is read, step (5) performs two tasks: adjusts the threshold level and normalizes the signal delivered by the rear sensor, enforcing Eq. (37), and classifies the front and rear sensor normalized signals accordingly to Section 3.4. Step (6) determines the local PDFs for the apparent bubble velocity and chord length, Eqs. (2) and (4), as well as its first and second moments. In step (7) the averaged and the mean square values of the velocity and chord length ratios are evaluated by means of Eqs. (12) and (13). Initial guesses for $\bar{D}$ and γ_0 are used to start the procedure: $\bar{D} = \bar{X}_s$ and $\gamma_0 = 0$. They are necessary since the first and second moments of $p(V_s/V_b)$ and $p(X_s/D)$ depend on $\bar{D}$ and γ_0. In step (8) a

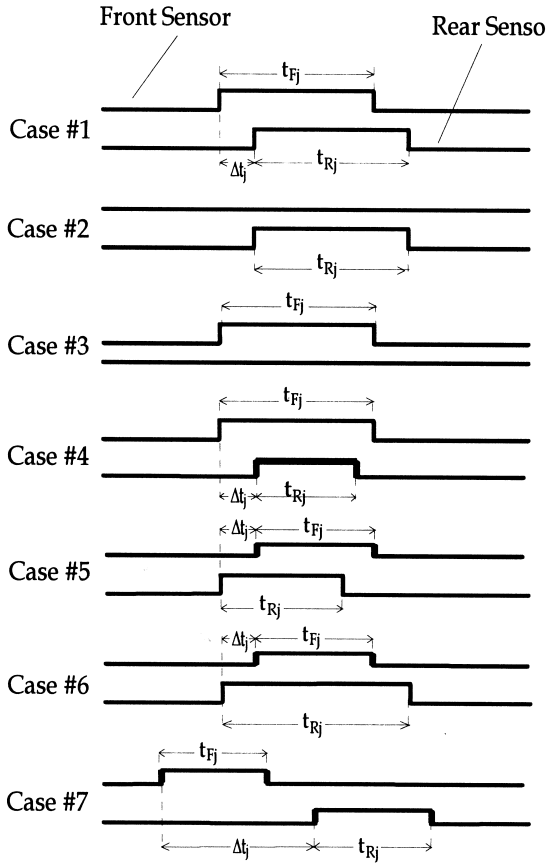

Fig. 13. Classification of the signals generated by the two sensors.

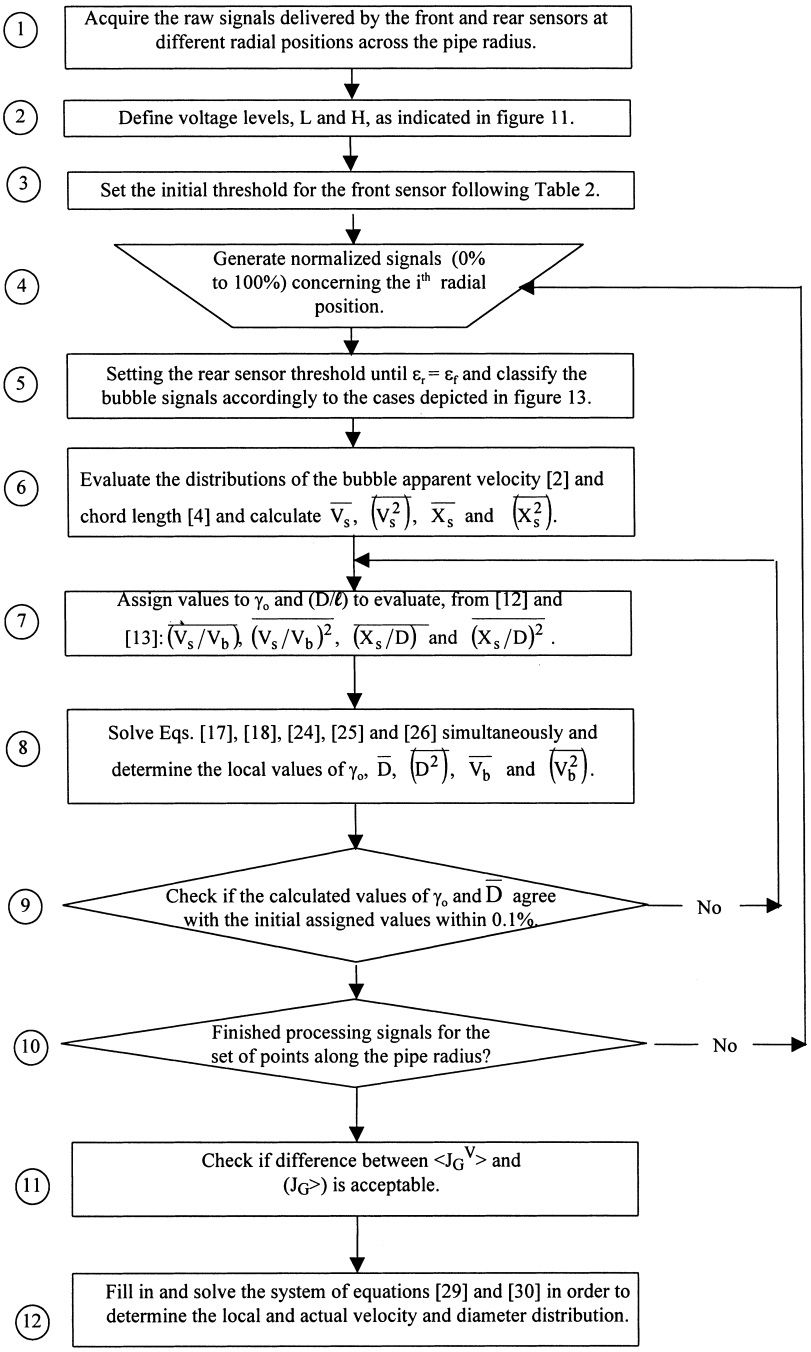

Fig. 14. Flow chart diagram for the determination of local PDFs.

system of non-linear algebraic equations; Eqs. (17), (18) and (24) through (26), is solved interactively to get the values of γ_0, $\bar{D}$, $\bar{D}^2$, $\bar{V}_b$ and $\bar{V}_b^2$ for the ith pipe radial position. The step (9) checks if the relative differences between $\bar{D}$ and γ_0, as calculated in step (8), are used in step (7) to repeat the calculations; otherwise, the next data is read. When the entire set of data points has been processed, step (10) switches the process to step (11). A direct comparison between the estimated superficial gas velocity, Eq. (38), and volumetric measurement is made in step (11) to be alert for miscalculations or data problems. The difference between the estimated and measured values was always less than 8.5%. A graphical comparison for the entire set of data points will appear in Section 4.1. Then, the procedure exits with a converged solution for the limiting entrance angle, and the mean and variance of the actual bubble velocity and bubble diameter. As a final remark, it is important to state that the results do not depend on the initial guesses for $\bar{D}$ and γ_0, the final solution satisfying a system of algebraic equations.

4. Results

Eighteen runs were carried out to generate experimental data of typical variables in upward two-phase bubbly flows. In every run, corresponding to a pair of gas and liquid superficial velocities, (J_G; J_L), the measurements were taken at ten different radial positions along the pipe radius, summing up one hundred eighty data points. The air and water superficial velocities ranged from $\langle J_G \rangle = 1.0$ cm/s to 14.2 cm/s, and from $\langle J_L \rangle = 0$ cm/s to 103 cm/s, respectively. The results shown in this section report some of the data available; the full set is found in Dias (1998)

The still pictures taken at the test section reveal that the bubbles are not spherical, but slightly distorted (see Fig. 15). Their diameters lay within the range of 2.5 mm to 4.0

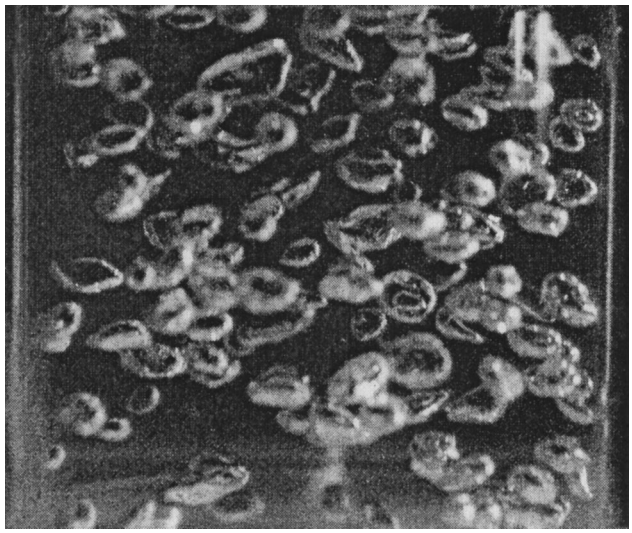

Fig. 15. Test section photograph: $\langle J_L \rangle = 103$ cm/s and $\langle J_G \rangle = 7.0$ cm/s

Table 3
Local data for $\langle J_L \rangle = 103$ cm/s and $\langle J_G \rangle = 7.0$ cm/s

r/R	ε(%)	$\bar{V}_s$ (m/s)	$\bar{V}_b$ (m/s)	σ_{V_b} (m/s)	$\sigma_{V_b}/\bar{V}_b$ (%)	$\bar{X}_s$ (mm)	$\bar{D}$ (mm)	σ_D (mm)
0.95	14.2	1.19	1.17	0.04	3.4	2.1	3.0	0.7
0.90	7.5	1.29	1.28	0.08	6.2	2.1	3.0	0.5
0.85	6.5	1.34	1.34	0.11	8.2	2.2	3.1	0.4
0.80	5.4	1.38	1.37	0.11	8.0	2.1	3.0	0.5
0.70	4.0	1.41	1.40	0.11	7.8	2.1	3.0	0.5
0.60	3.3	1.41	1.39	0.09	6.4	2.0	2.9	0.5
0.50	2.9	1.41	1.40	0.12	8.5	2.1	2.9	0.5
0.30	2.6	1.39	1.37	0.09	6.5	2.0	2.8	0.5
0.10	2.3	1.38	1.37	0.11	8.0	1.9	2.7	0.4
0.00	2.2	1.35	1.34	0.09	6.7	1.9	2.6	0.4
< >	5.0	1.30	1.28			2.0	2.9	

mm. For reference, the data of three selected runs are presented in Tables 3–5. For 10 radial positions along the pipe radius, they display: the local void fraction, ε, the averaged values of the apparent and actual bubble velocity; the actual velocity standard deviation, σ_{V_b}; the interface velocity fluctuation intensity, defined as the ratio between standard deviation and mean actual velocity, $\sigma_{V_b}/\bar{V}_b$; the mean chord length, the mean bubble diameter and the standard deviation of the bubble diameter, void fraction, apparent velocity, actual velocity, intersected chord and bubble diameter. Finally, the last row brings some area averaged values under the symbol $\langle\ \rangle$.

For two out of three selected runs, $\langle J_L \rangle = 51$ cm/s and $\langle J_L \rangle = 103$ cm/s, the data display the typical local void fraction peak near the wall (see Tables 3 and 4). Similar saddle shape distributions were obtained by Serizawa et al. (1975b) and Wang et al. (1987). For $\langle J_L \rangle = 0$ cm/s, however, the void fraction distribution does not show any wall-peaking and is rather flat. The averaged value of the apparent velocity is always higher than the actual velocity; both

Table 4
Local data for $\langle J_L \rangle = 51$ cm/s and $\langle J_G \rangle = 5.0$ cm/s

r/R	ε(%)	$\bar{V}_s$ (m/s)	$\bar{V}_b$ (m/s)	σ_{V_b} (m/s)	$\sigma_{V_b}/\bar{V}_b$ (%)	$\bar{X}_s$ (mm)	$\bar{D}$ (mm)	σ_D (mm)
0.95	8.8	0.70	0.66	0.07	10.0	2.3	3.1	0.6
0.90	9.3	0.71	0.70	0.06	8.5	2.3	3.2	0.6
0.85	8.6	0.75	0.74	0.06	8.0	2.3	3.3	0.6
0.80	7.5	0.79	0.78	0.05	6.3	2.4	3.3	0.6
0.70	6.7	0.78	0.78	0.07	9.0	2.3	3.2	0.6
0.60	6.0	0.79	0.78	0.05	6.3	2.3	3.3	0.4
0.50	5.7	0.74	0.74	0.03	4.1	2.3	3.2	0.4
0.30	5.7	0.75	0.75	0.02	2.7	2.3	3.2	0.4
0.10	5.8	0.75	0.75	0.02	2.7	2.3	3.3	0.5
0.00	5.6	0.73	0.73	0.03	4.1	2.3	3.2	0.5
< >	6.7	0.72	0.71			2.3	3.3	

profiles exhibit the smallest values near the wall, as one would expect. The standard deviation of the actual velocity does not show a definite trend for the three selected runs. For $\langle J_L \rangle = 103$ cm/s and $\langle J_G \rangle = 7.0$ cm/s, it is nearly constant at the pipe center, and has a tendency to decrease as the wall is approached. For $\langle J_L \rangle = 51$ cm/s and $\langle J_G \rangle = 5.0$ cm/s there is no clear tendency. Finally, for $\langle J_L \rangle = 0$ cm/s and $\langle J_G \rangle = 1.0$ cm/s, one observes large oscillations.

The interface velocity fluctuation intensity stays, typically, within 2.6 to 10% for the data taken at $\langle J_L \rangle = 103$ cm/s and $\langle J_L \rangle = 51$ cm/s. These values are smaller than the ones found by Serizawa et al. (1975b), who reported typical values ranging from 10 to 15%. This is due to the fact that they calculated this variable for the bubble apparent velocity, which has a higher standard deviation than the actual velocity, a one used in this work. The interface velocity fluctuation intensity, however, changes significantly for $\langle J_L \rangle = 0$ cm/s, attaining values upto 40%. This is in agreement and is explained by the reasoning put forward by Serizawa et al. (1975b): as the water velocity increases, the fluctuating motion of the bubbles suspended in the stream becomes relatively suppressed by the intensified inertial force of the water.

The averaged chord length and bubble diameter radial profiles do not display any particular characteristic. As expected, the averaged chord length is always smaller than the bubble diameter. Also, the radial deviation on both averaged profiles, from the wall to the pipe center, stays within tenths of millimeter apart. The standard deviation of the bubble diameter lays within 0.3 to 1.0 mm, the highest local values coming out from the run $\langle J_L \rangle = 0$ cm/s and $\langle J_G \rangle = 1.0$ cm/s.

Fig. 16 shows a distribution of the apparent and actual velocity, $p(V_s)$ and $p(V_b)$, as well as the distribution of the chord length and bubble size (or bubble diameter), $p(X_s)$ and $p(D)$, taken at the pipe center line, $r/R = 0$, for five pairs ($\langle J_L \rangle$; $\langle J_G \rangle$). One notices that the distribution of the actual velocity is narrower than the apparent one. Also, as one would expect, the distribution of the bubble diameter is narrower than the distribution of the chord length.

Fig. 17 displays the radial profile of five interfacial variables: void fraction, bubble frequency, bubble velocity, bubble diameter and interfacial area density. These data correspond

Table 5
Local data for $\langle J_L \rangle = 0$ cm/s and $\langle J_G \rangle = 1.0$ cm/s

r/R	ε(%)	$\bar{V}_s$ (m/s)	$\bar{V}_b$ (m/s)	σ_{V_b} (m/s)	$\sigma_{V_b}/\bar{V}_b$ (%)	$\bar{X}_s$ (mm)	$\bar{D}$ (mm)	σ_D (mm)
0.95	1.1	0.28	0.26	0.07	25.0	3.0	3.6	1.0
0.90	1.5	0.30	0.25	0.12	40.0	3.0	3.4	0.6
0.85	1.7	0.28	0.25	0.08	28.6	2.7	3.2	0.5
0.80	1.8	0.33	0.29	0.09	27.3	2.7	3.3	0.6
0.70	1.8	0.33	0.31	0.04	12.1	2.7	3.5	0.8
0.60	1.8	0.33	0.29	0.08	24.2	2.6	3.2	0.7
0.50	1.4	0.36	0.34	0.09	25.0	2.8	3.4	0.8
0.30	1.4	0.31	0.28	0.08	28.6	2.6	3.3	0.5
0.10	1.5	0.34	0.32	0.10	29.4	2.6	3.1	0.9
0.00	1.3	0.33	0.29	0.09	31.0	2.8	3.4	0.9
< >	1.5	0.30	0.28			2.7	3.4	

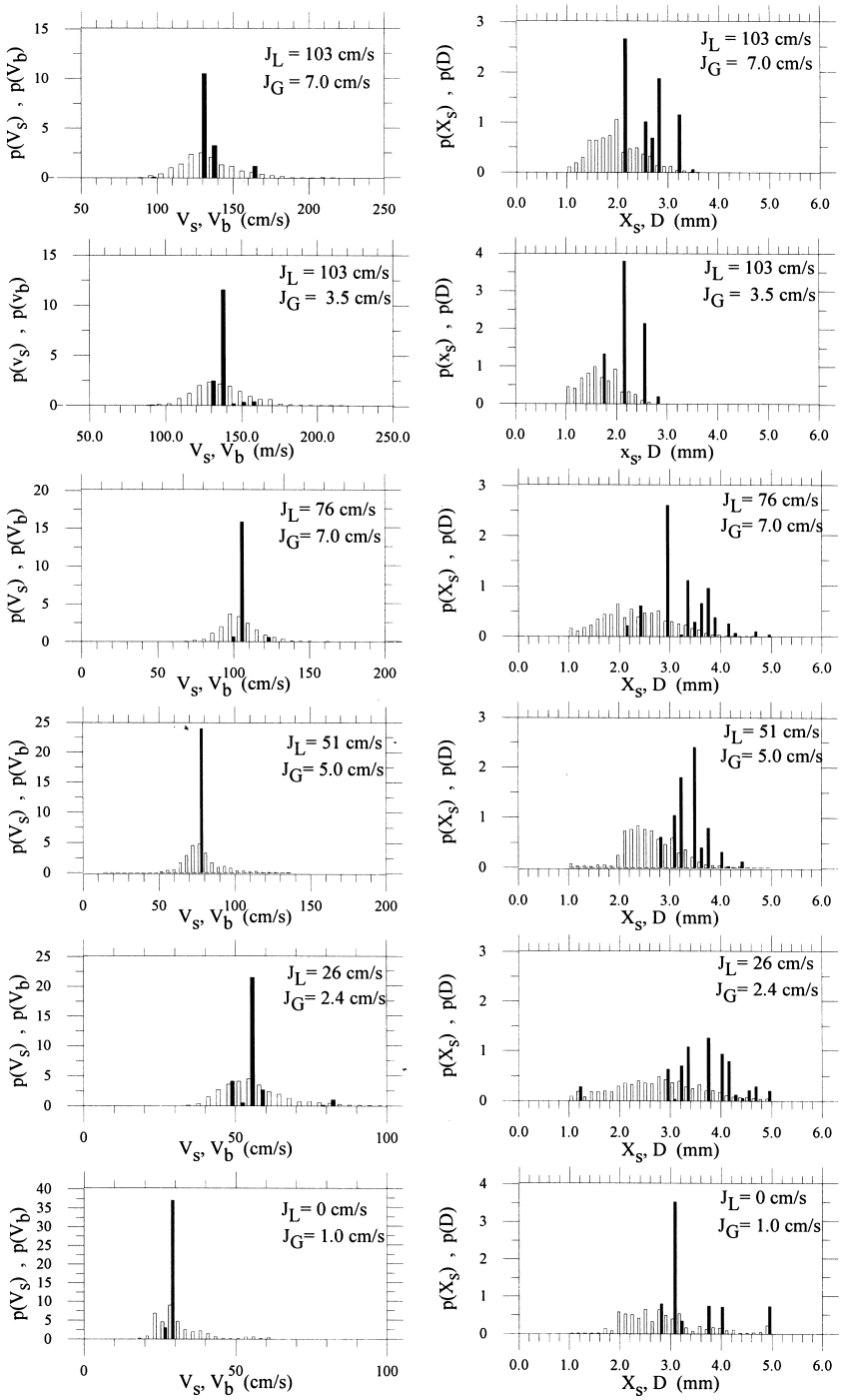

Fig. 16. PDF of the apparent and actual bubble velocity, in cm/s, and of the chord length and bubble diameter, in mm, at pipe center, $r/R = 0$, for different liquid and gas superficial velocities. Open rectangles, □ applies to $p(V_s)$ or $p(X_s)$; solid rectangles ■ applies to $p(V_b)$ or $p(D)$.

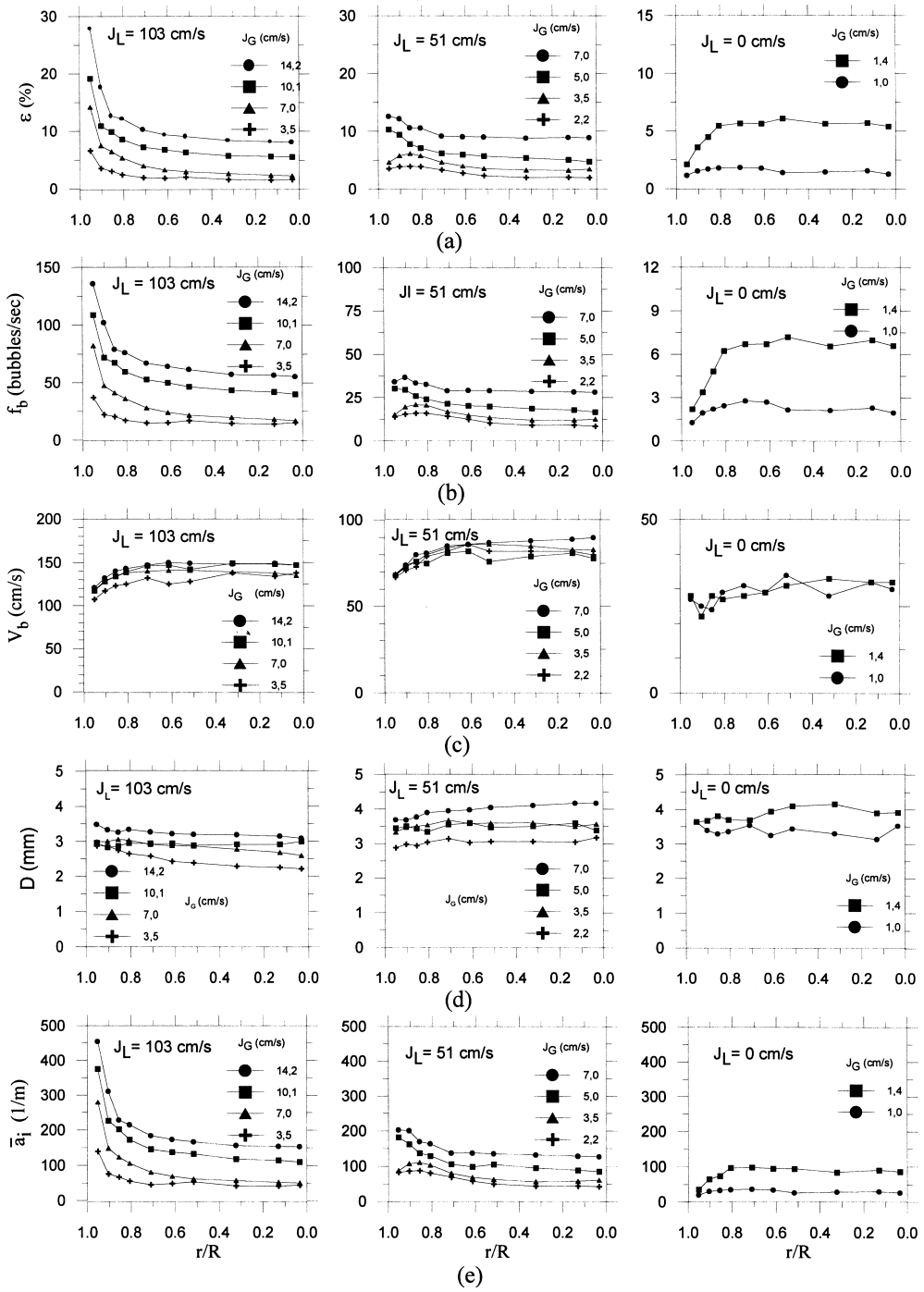

Fig. 17. Radial profiles of: (a) void fraction; (b) bubble frequency; (c) bubble velocity; (d) bubble diameter and (e) interfacial area density.

to $\langle J_L \rangle$ equals to 103 cm/s, 51 cm/s, 0 cm/s and $\langle J_G \rangle$ spanning from 1.0 cm/s to 14.2 cm/s. The radial profile of the void fraction, shown in Fig. 17(a), depends primarily on the liquid flow rate. For $\langle J_L \rangle = 103$ cm/s, the radial distribution exhibits the typical void peaking near the wall, as remarkably as the gas flow rate increases, in a similar fashion to the Serizawa et al. (1975a) and Wang et al. (1987) data. For $\langle J_L \rangle = 51$ cm/s the void fraction distribution depends on the gas flow rate: it shows the wall peaking when $\langle J_G \rangle$ is equal or greater than 5.0 cm/s; for lower gas superficial velocities, the profiles get a convex shape close to the pipe wall, but are rather flat in the pipe center region. When $\langle J_L \rangle = 0$ cm/s, the void fraction shows a definite reduction close to the wall and its profile is entirely convex. The radial distribution of the bubble frequency, as defined by Eq. (35), is shown in Fig. 17b. The profiles are similar to the void fraction profiles at distinct liquid flow rates. They attain rates up to 130 bubbles per second, when $\langle J_L \rangle = 103$ cm/s; $\langle J_G \rangle = 14.2$ cm/s, or as low as 1.5 bubbles per second when $\langle J_L \rangle = 0$ cm/s, $\langle J_G \rangle = 1$ cm/s.

The average bubble velocity, as shown in Fig. 17(c), has a nearly flat distribution in the pipe core region, decreasing, as one would expect, near the pipe wall. This is valid for the entire set of gas and liquid superficial velocities, besides showing some oscillations when $\langle J_L \rangle = 0.0$ cm/s. Looking at the void fraction and frequency distributions when $\langle J_L \rangle = 103$ cm/s, one alludes to the fact that the pronounced wall peaking in void fraction must be the combination of a relatively higher frequency of bubbles displacing at lower velocities. When ($\langle J_L \rangle = 103$ cm/s; $\langle J_G \rangle \geq 5.0$ cm/s), the less pronounced frequency peak, with regard to the central region, causes a less pronounced peaking in the void fraction. When $\langle J_L \rangle = 0.0$ cm/s, the frequency profile forges the convex shape of the void fraction distribution.

The radial profiles of the average bubble diameter are shown in Fig. 17(d). The profiles are rather flat, but the bubble diameter increases slightly toward the wall at the higher liquid flow rate, $\langle J_L \rangle = 103$ cm/s. The average bubble diameter is within 2.2 mm to 4.2 mm, confirming the sizes depicted in the still picture. One also notices that the bubbles tend to grow as $\langle J_G \rangle$ increases at a constant $\langle J_L \rangle$. Otherwise, the bubble diameter diminish as $\langle J_L \rangle$ increases. These two effects must be related to the bubble generation processes occurring in the air–water chamber.The interfacial area density distribution is shown in Fig. 17(e). Following Ishii (1975), one writes the interfacial area density, a_i, in terms of the bubble velocity and frequency. The expression is valid if the flow is steady and developed:

$$a_i = 2f_b \overline{\frac{1}{|V_b| \cos \phi}}, \tag{40}$$

The PDF of the conical angle, $p(\phi)$, is given by Eq. (14). If the conical angle and the bubble velocity are statistically independent events, Eq. (40) simplifies to

$$a_i = 2f_b \overline{\left(\frac{1}{|V_b|}\right)} \cdot \overline{\left(\frac{1}{\cos \phi}\right)}. \tag{41}$$

The interfacial area density profiles are, again, quite similar to the frequency profiles, reflecting the fact that the radial change in frequency is stronger than the change in velocity.

In addition to these local interfacial variables, one calculated two other quantities, averaged over the pipe cross section, namely, the bubble-size frequency spectrum, i.e., the distribution of

bubble frequency over the full range of bubble diameter, $f_D(D)$, and the bubble-size probability function, which gives the probability of finding a bubble with a given diameter D in the pipe cross section, $p_{\langle\rangle}(D)$. Noticing that the probe gets information over a region of influence around its tip, which is proportional to the bubble diameter, the probability of intercepting a bubble of diameter D inside the pipe is the ratio between the bubble and the pipe cross section area. Then, if the bubble frequency is a local quantity, $f_b = f_b(r)$, as well as the bubble size distribution function $p(D, r)$, the frequency of bubbles with diameter D in the pipe cross-section, $f_D(D)$, is:

$$f_D(D) = \int_0^R 2\pi r \left[\left(\frac{f_b(r)}{\pi D^2/4} \right) p(D, r) \right] dr, \tag{42}$$

From Eq. (42), one is able to define the total bubble frequency, $f_{\langle\rangle}$, in the pipe cross section:

$$f_{\langle\rangle} = \int f_D(D)\, dD. \tag{43}$$

Finally, the averaged bubble-size PDF $p_{\langle\rangle}(D)$ is the ratio between Eqs. (42) and (43):

$$p_{\langle\rangle}(D) = \frac{f_D(D)}{f_{\langle\rangle}} \tag{44}$$

Three averaged bubble-size PDFs, $p_{\langle\rangle}(D)$, calculated according to Eq. (44), are shown in Fig. 18. One notices that the smaller bubbles are more likely to occur. If the probability of intercepting a bubble of diameter D inside the pipe is proportional to the square of the bubble to pipe diameter, Eq. (42), the bubble-size frequency spectrum will indicate that the smallest bubbles will have the highest frequencies. This reasoning explains the difference in the bubble spectrum if one compares the results in Fig. 18 with the local PDFs shown in Fig. 17(d). As

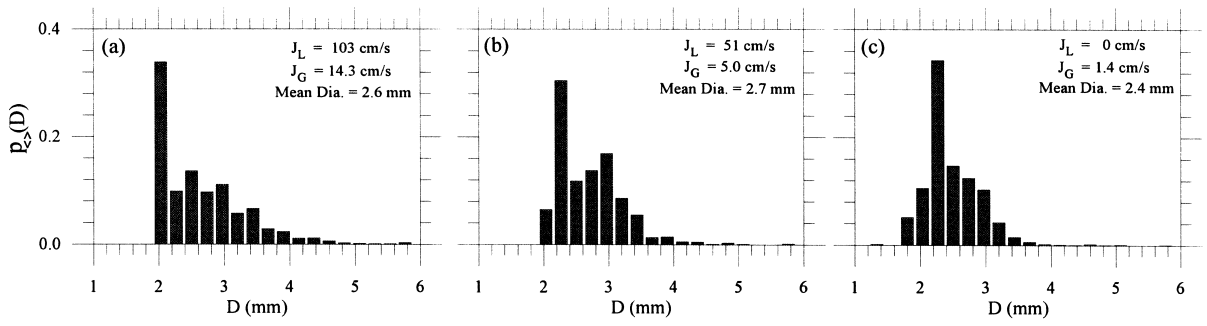

Fig. 18. Averaged bubble-size probability density function.

one may observe, the mean bubble diameter in Fig. 18(a)–(c) is, respectively, 2.6, 2.7 and 2.4 mm. The local PDFs reveal 3.3, 3.5 and 3.8 mm.

4.1. Validation

The agreement of the results obtained in this work with previously published ones validates the model. A further validation, however, is achieved when one compares volumetric measurements with quantities coming out from area averaging processes, or when one compares the results with a extensively used relation. In the former case, the gas superficial velocity, as measured by the orifice plate, is compared with averaged values calculated from the local measurement of the interfacial properties, namely, the superficial gas velocity calculated as the product of the interfacial velocity and the void fraction, given by Eq. (38), or as the product of the bubble volume times the bubble frequency, both averaged over the pipe section. These alternative forms to evaluate $\langle J_G \rangle$ are used to check the consistency of the method. In the latter case, the radial distribution of the interfacial area density is compared with the well known equation proposed by Ishii and Mishima (1984), which is valid under some restrictions.

The gas superficial velocity, expressed in terms of the bubble frequency and volume, is then:

$$\langle J_G^D \rangle = f_{\langle\rangle} \int p_{\langle\rangle}(D) \frac{\pi D^3}{6} \, dD, \tag{45}$$

where $f_{\langle\rangle}$ is defined in Eq. (43).

Fig. 19(a) shows, for reference, the superficial gas velocity, measured with the orifice plate, against $\langle J_G^V \rangle$, as given by Eq. (38). The agreement is bounded within 8,5%. Fig. 19(b) shows

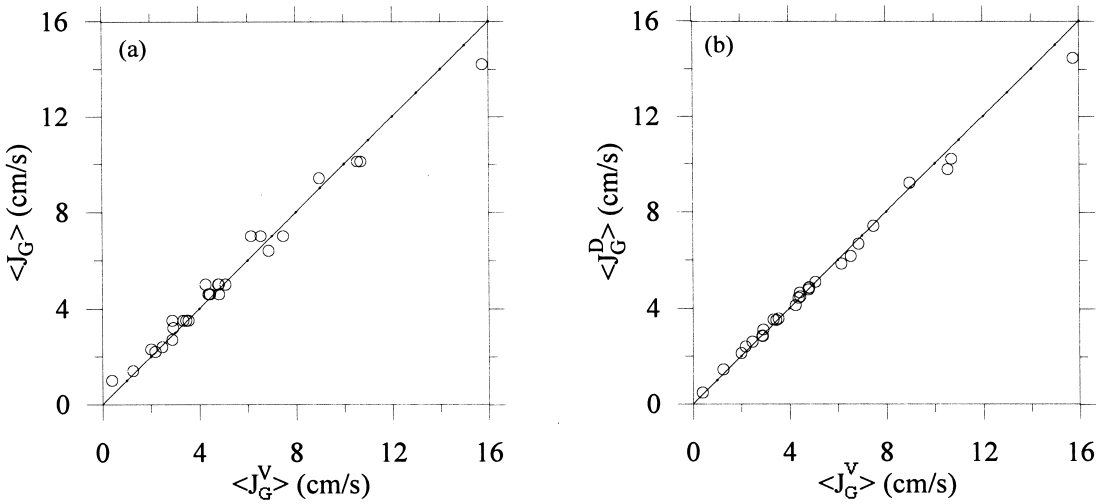

Fig. 19. Area averaged superficial gas velocity comparisons: (a) volumetric measurement, $\langle J_G \rangle$, against the averaged gas superficial velocity, $\langle J_G^D \rangle$, and (b) the gas superficial velocity, expressed in terms of the bubble frequency and volume, $\langle J_G^D \rangle$, against $\langle J_G^V \rangle$.

the plot of the gas superficial velocity $\langle J_G^D \rangle$, as given in Eq. (45), against $\langle J_D^V \rangle$. In this case the dispersion is tighter indicating that both formulae give results bounded within 8.5% in regard to $\langle J_G \rangle$.

The uncertainty of $\langle J_G \rangle$ may be as high as 2.5% due to the combined uncertainty of the measurements taken with the orifice plate, 2%, and the Plexiglas pipe cross section area, at least 1.5%. Putting this into perspective, the bound of 8.5% is considered a good result, emphasizing the consistency of the method.

Following Ishii and Mishima (1984), the local interfacial area concentration, a_i^D is calculated from

$$a_i^D(r) = \frac{6\varepsilon(r)}{D_{SM}(r)}, \tag{46}$$

where the Sauter mean diameter, D_{SM}, is

$$D_{SM}(r) = \frac{\int p(D) D^3 \, dD}{\int p(D) D^2 \, dD}. \tag{47}$$

A direct comparison between the two radial profile, as calculated by Eqs. (41) and (46), is shown in Fig. 20 for three different runs. The open symbols refer to Eq. (41), the closed ones to Eq. (46). The agreement, again, is very good showing the coherence of the measurements.

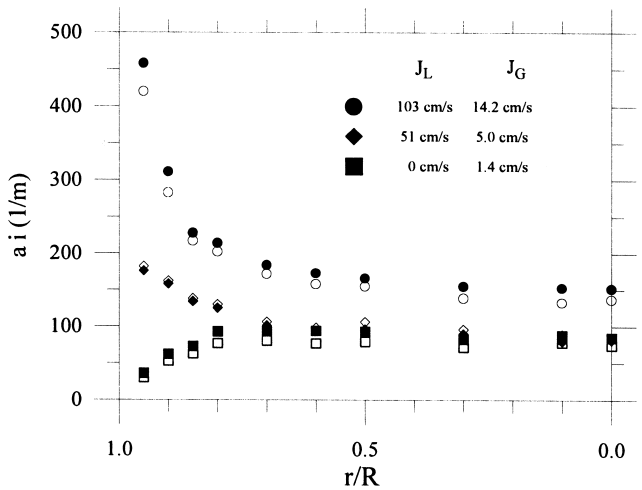

Fig. 20. Interfacial area concentration. The open and closed symbols refer to a_i as evaluated using Eq. (41) or Eq. (46), respectively.

5. Conclusions

A new statistical method aimed to calculate of local interfacial variables in two-phase gas–liquid bubbly flows was developed. The method applies to data taken with double-sensored intruse probes. The analysis first considered a single spherical bubble and was further extended, as a statistical approach, to a swarm of bubbles. The basic assumption of the method accounted for the multidimensional nature of bubble displacement. In this less restrictive flow, the analysis related the measured or apparent variables, the bubble velocity and intersected chord, with the actual ones.

To verify the consistency of the method, a large number of data were taken. An experimental apparatus was constructed to generate bubbly flow in a vertical round pipe. The interfacial properties were measured with a double-sensor electrical probe. The approach employed for data conversion and interpretation treats the signals generated by the two sensors separately in order to construct the phase indicator functions. The mean residence time, the void fraction and the bubble frequency delivered by each sensor are taken into account before setting a generic threshold level. A further adjustment of the threshold setting is achieved by taking the difference between the measured and calculated averaged gas superficial velocity.

The method was validated comparing the radial distribution of local variables, like the void fraction, the bubble velocity or the interface velocity fluctuation intensity, with previously published ones. A further validation was achieved comparing the results with extensively used relationships, as the one for interfacial area density, or comparing volumetric measurements with quantities coming out from area averaging processes. In the latter case the deviation bounds within 8.5%. This deviation is largely due to the intrusive nature of the measurements, to the non-spherical bubble inclusions and to the uncertainty in the measurement of the gas superficial velocity. The bubble piercing process is complex. It may ultimately alter the void fraction and the bubble velocity due to deceleration, deformation and trajectory shift. The method, despite being developed for spherical bubbles, was tested in bubble populations which exhibited spherical and non-spherical shapes. A clear accountancy of these processes on the limit of validity of the model is beyond the scope of this work. However, most of the mentioned deviation regarding volumetric measurements can be attributed to the net result of these processes. The method proved to be computationally efficient and disclosed physically consistent results for the actual distribution of the bubble velocity and size.

One of the most important characteristics revealed by the method is concerned with the difference between the measured and the actual PDF of the bubble velocity and bubble diameter. In fact, one may emphasize that the PDFs of the actual variables, bubble velocity or diameter, are narrower than the respective PDFs of the measured variables (Fig. 15). Different from what is reported by Serizawa et al. (1975b) or Kocamustafaogullari and Wang (1991), this effect is remarkable for the velocity distribution: the actual bubble velocity is almost constant, contrasting with a measured velocity that presented a wider spectrum.

The method also described well the influence of the entrance angle on the deviation between the apparent and actual distribution. The mean apparent bubble velocity equals the actual one only if γ_0, the limiting angle, is zero; otherwise, the velocity ratio increases with increasing γ_0. If the entrance angle is constant, the velocity ratio is always bigger than one. Also, it is bigger than the velocity ratio that comes out when one assumes an entrance angle uniformly

distributed within a solid angle. Even though the analysis relied strongly on the entrance angle aspects, this is still a subject of further research. For example, the hypothesis of isotropy postulated by Kataoka et al. (1986) to relate to the flow characteristics is questionable in regions near the wall. Also, more simple questions relating the entrance angle with bubbly flow patterns, are not fully established yet.

Another important aspect disclosed in this study is the influence of the probe lengthwise spacing on the deviation between the measured and actual variables. When D/ℓ increases, the standard deviation of the statistical distributions also increases (velocity or intersected chord length). Therefore, measurements made with probes having high D/ℓ are likely to display a wider spectrum than the ones carried with probes having smaller D/ℓ. The mean values, however, do not change significantly.

Acknowledgements

The authors acknowledge Petrobras for supporting this work. They also express their appreciation to Mr. S.C. Collucci, wo designed and performed the final adjustments in the electronic circuit which drove the double sensor probe.

References

Bachalo, W.D., 1994. Experimental methods in multiphase flows. Int. J. Multiphase Flow 20, 261–295.

Cartellier, A., Achard, J.L., 1991. Local phase detection probes in fluid/fluid two-phase flows. Rev. Sco. Instrum 62 (2), 279–303.

Dias, S.G., 1998. Distribuição de Fases em Escoamentos com Simetria Axial em Padrão Bolhas: Aplicação do Modelo de Dois Fluidos e Comprovação Experimental com Novo Méstodo Usando a Sonda Dupla (in Portuguese). PhD Thesis. Faculty of Mechanical Engineering, State University of Campinas, UNICAMP, Brazil.

Delhaye, J.M., Galaup, J.P., 1974. Measurement of local void fraction in Freon 12 with a 0.1 mm optical fiber probe. In: European Two-Phase Flow Meeting, Harwell, England.

Hilgert, W., Hoffmann, H., 1986. Characterization of gas phase flow in bubble columns of low superficial gas velocities with the aid of ultrasonic doppler techniques. Gen. Chem. Engng 9, 180–190.

Herringe, R.A., Davis, M.R., 1976. Structural development of gas–liquid mixture flows. J. Fluid Mech 73, 97–123.

Ishii, M., 1975. Thermo-Fluid Dynamics Theory of Two-Phase Flow. Eyrolles, France.

Ishii, M., 1977. One-Dimensional Drift-Flux Model and Constitutive Equations for Relative Motion Between Phases in Various Two-Phase Regimes. Argonne National Laboratory, pp. 77, 47.

Ishii, M., Mishima, K., 1984. Two-fluid model and hydrodynamic constitutive relations. Nuclear Engng. and Design 82, 107–126.

Kataoka, I., Ishii, M., Serizawa, A., 1986. Local formulation and measurements of interfacial area concentration in two-phase flow. Int. J. Multiphase Flow 12, 505–529.

Kocamustafaogullari, G., Wang, Z., 1991. An experimental study of local interfacial parameters in a horizontal bubbly two-phase flow. Int. J. Multiphase Flow 17, 553–572.

Leung, W., Revankar, S., Ishii, Y., Ishii, M., 1995. Axial development of interfacial area and void concentration profiles measured by double-sensor probe method. Int. J. Heat Mass Transfer 38, 445–453.

Liu, W., Clark, N.N., 1995. Relationships between distribution of chord lengths and distribution of bubble sizes including their statistical parameters. Int. J. Multiphase Flow 21, 1073–1089.

de Bertodano, Lopez, 1992. Turbulent bubbly two-phase flow in a triangular duct. In: 5th Intern. topical Meeting on Nuclear Reactor Thermal Hydraulics, Salt Lake City, UT, USA, Sept. 20-24.

Saffman, B.G., 1956. On the rise of small air bubbles in water. J. Fluid Mech 3, 249–275.
Serizawa, A., Kataoka, I., Michiyoshi, I., 1975a. Turbulence structure of air–water bubbly flow. Part I: Measuring techniques. Int. J. Multiphase Flow 2, 221–234.
Serizawa, A., Kataoka, I., Michiyoshi, I., 1975b. Turbulence structure of air–water bubbly flow. Part II: Local properties. Int. J. Multiphase Flow 2, 235–246.
Wang, S.K., Lee, S.J., Jones, O.C., Lahey, R.T., 1987. 3D turbulence structure and phase distribution measurements in bubbly two-phase flows. Int. J. Multiphase Flow 13, 327–343.